Diagnostic performance of photoplethysmography for early vascular compromise in a customisable *in vitro* flap model

Medical Engineering & Physics

IPEM Institute of Physics and Engineering in Medicine

PAPER

Diagnostic performance of photoplethysmography for early vascular compromise in a customisable *in vitro* flap model

Hiroki Kodama[1,2,3,*], **James M May**[2,4], **Dariush Nikkhah**[1] **and Panicos A Kyriacou**[2]

[1] Research Centre for Biomedical Engineering, City St George's, University of London, London, United Kingdom
[2] Department of Plastic and Reconstructive Surgery, Royal Free London NHS Foundation Trust, London, United Kingdom
[3] Department of Plastic and Reconstructive Surgery, The Jikei University School of Medicine, Tokyo, Japan
[4] Division of Surgery and Interventional Science, University College London, London, United Kingdom
[*] Author to whom any correspondence should be addressed.

E-mail: Hiroki.kodama.2@city.ac.uk

Keywords: free flap, photoplethysmography (PPG), phantom study, plastic surgery, biomedical engineering, wearable device

OPEN ACCESS

RECEIVED
6 March 2026

REVISED
13 May 2026

ACCEPTED FOR PUBLICATION
2 June 2026

PUBLISHED
11 June 2026

Abstract

Background: Free flap reconstruction is a standard procedure in surgery, yet vascular thrombosis occurs in 3%–5% of cases. Early detection within the first few hours is essential for successful salvage, as the success rate of surgical re-exploration decreases over time. Since current clinical assessment remains subjective and depends on experience, objective and continuous monitoring is required. Photoplethysmography (PPG), which monitors blood volume changes non-invasively, is a candidate for this application. However, the influence of specific waveform changes during early haemodynamic shifts is not fully understood. Methods: This study evaluated the diagnostic capacity of PPG for detecting early vascular changes using a custom silicone phantom. Synthetic vessels mimicking human arterial and venous mechanics were embedded at depths of 3, 9, 15, and 21 mm. A perfusion system simulated normal, early ischaemic, and early congested states. Signal quality was assessed using the signal-to-noise ratio (SNR), and only signals with SNR $>$ 15 dB were used for morphological analysis. Over 50 parameters, including time, area, and slope, were extracted from the waveforms to identify those that characteristically respond to each haemodynamic state. Results: The custom-made free flap phantom was successfully validated. Signal quality assessments limited morphological evaluation to depths up to 15 mm. Analysis showed that Intensity and Area-based parameters were the most effective indicators at all depths. At shallow positions, Time-related features showed clear changes during ischaemia, while Slope and Second Derivative (SDPPG) features emerged as key indicators at depth. Red light was useful for superficial monitoring at 3 mm, whereas Infrared was necessary for assessing deeper states. Conclusion: A custom phantom capable of replicating early haemodynamic compromise was developed. Identifying specific feature variations across depths provides a framework for objective, continuous monitoring. These findings suggest that combining multiple morphological features can improve the reliability of flap assessment.

1. Introduction

Free flaps are tissue units transferred from a donor to a recipient site while maintaining their original blood supply via microvascular anastomosis (connection between two blood vessels). Free flap reconstruction represents a cornerstone method for managing large and complex defects, offering superior functional and aesthetic outcomes in diverse anatomical locations, including the head and neck (Nakatsuka *et al* 2003), breast (Harashina *et al* 1980), and extremities (Taylor *et al* 1975). The procedure's growing importance is evidenced by national data; for example, a 2020 report from the United States indicated that the number of free flap procedures performed for breast reconstruction reached 23 324, representing a 75% increase over the preceding two decades (American Society of Plastic Surgeons 2020).

Despite the substantial benefits of microvascular tissue transplantation, blood flow deficits remain a significant concern, occurring in approximately 3%–5% of cases (Nakatsuka *et al* 2003, Caine *et al* 2023). Vascular thrombosis is the principal risk factor, typically manifesting within the first 48 h post-surgery (Kroll *et al* 1996, Bui *et al* 2007, Tran *et al* 2007), A severe consequence of delayed diagnosis is a significantly reduced probability of free flap salvage. Furthermore, the need for a second flap to address failure is reported to incur an additional cost of $174 000 (Mericli *et al* 2017). Crucially, historical studies report that prompt salvage surgeries initiated within the first 24 h of vascular compromise successfully save 70%–80% of affected flaps (Disa *et al* 1999, Chen *et al* 2007, Al-dam *et al* 2014, Caine *et al* 2023).

The traditional method of clinical assessment remains the established standard for evaluating free flaps and achieving early detection of compromise. This evaluation includes measurements of skin colour, capillary refill time, tissue fullness (turgor) caused by fluid build-up, perceptible by the physical examination of how hard or soft the tissue is, temperature, and pinprick response. However, these observations are labour-intensive, as they must be performed manually and frequently (Patel *et al* 2017). Furthermore, these characteristics are qualitatively and subjectively monitored, largely depending on the expertise of the individual physician or nurse. Because different personnel often monitor the flap, inconsistencies may arise in these observations, risking the oversight of subtle changes (Patel *et al* 2017).

Various monitoring devices are currently available on the market. Pinpoint measurement, devices such as near-infrared spectroscopy (NIRS) (Kagaya and Miyamoto 2018), laser Doppler flowmetry (Kodama *et al* 2025), implantable Doppler probes (Wu *et al* 2023), flow couplers (Colakoglu *et al* 2020), and microdialysis (Hwang 2023) are utilised. For image-based assessment, techniques such as Indocyanine Green Fluorescence Angiography (Burnier *et al* 2017) and thermography Hudson *et al* (2023) are available. Each of these technologies possesses inherent strengths and limitations, and a universal consensus regarding their optimal clinical use does not currently exist (Kwasnicki *et al* 2021).

Among these continuous monitoring technologies, NIRS and Photoplethysmography (PPG) provide non-invasive optical assessments. NIRS is a well-established and mature technology that utilises multiple near-infrared wavelengths to estimate the concentration changes of oxygenated and deoxygenated haemoglobin, thereby directly evaluating the tissue oxygen supply-demand balance even in deeper layers (Kagaya and Miyamoto 2018). Conversely, PPG operates on a different principle as a volumetric measurement technique that captures variations in light intensity caused by pulsatile blood volume changes (Kyriacou 2022). The inherent strength of PPG lies in its high temporal resolution and exceptional sensitivity to dynamic arterial blood flow, making it highly suitable for beat-to-beat morphological waveform analysis. Furthermore, the compact nature and low power consumption of PPG sensors offer a high affinity for integration into wearable devices, facilitating long-term, continuous bedside monitoring (Charlton *et al* 2023). Such pulse wave morphological evaluation via PPG is increasingly gaining traction in various cardiovascular monitoring applications.

However, direct evidence regarding PPG's diagnostic performance and the specific alterations in pulse wave morphology during the early stages of free flap vascular compromise remains scarce (Kyriacou *et al* 2020, Zaman *et al* 2011). Therefore, the core objective of this study is to focus on the morphological features of PPG pulse waves in flap perfusion. Evaluating PPG's diagnostic capacity and morphological analysis is essential for advancing objective, continuous flap monitoring technology.

This study aims to determine measurement depth limits and validate PPG's performance for early free-flap blood flow changes using an *in vitro* vascular system. Identifying various pulse wave characteristics provides insights for future monitoring strategies.

2. Methods

2.1. Phantom creation and experimental setup

The experimental system was built using established Zen PPG hardware (Budidha *et al* 2018). To simulate free flap vasculature, custom-made silicone vessels were fabricated according to previous methods (Karimpour *et al* 2024, Ferizoli *et al* 2024) accurately mimicking the ΔCSA (Change in Cross-Sectional Area) and compliance reported in the literature (Cappelletti *et al* 2022). The general experimental circuit for PPG validation was modified to specifically model flap circulation, incorporating the fabricated vessels at varying depths within a tissue phantom. Intravascular pressure was precisely controlled to simulate the small artery and vein under specific conditions, including normal flow, early ischaemia, and early congestion. This setup allowed for an *in vitro* assessment by creating precise and reproducible flow abnormalities.

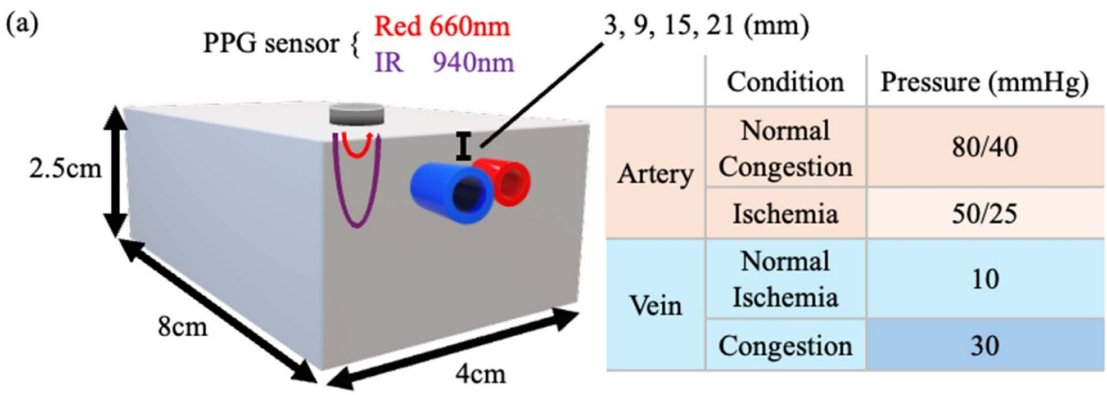

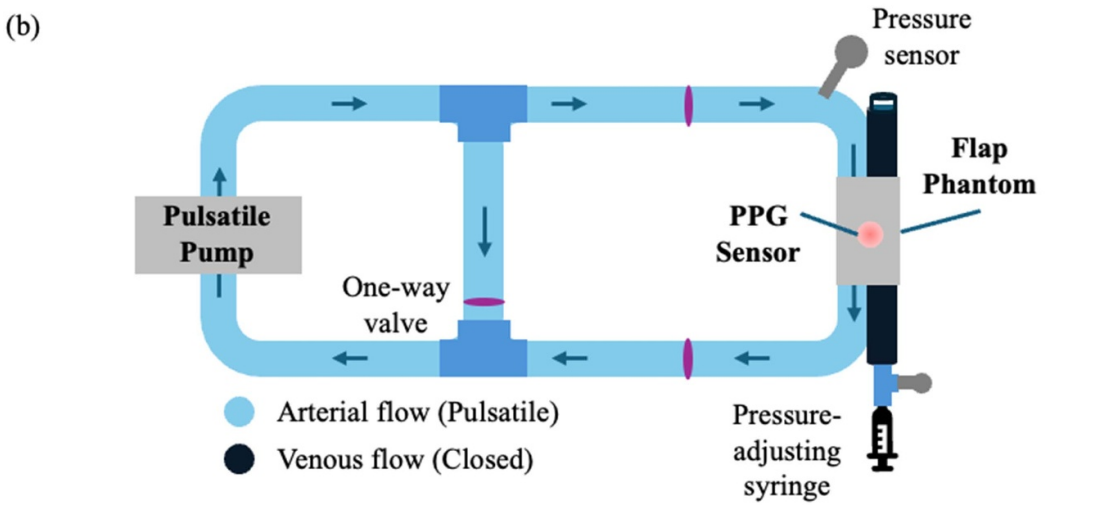

Figure 1. (a) Details of the fabricated phantom and experimental conditions. (b) Schematic diagram of the cardiovascular system. A PPG sensor is applied to a tissue phantom containing an artery connected to a pump and a vein connected to a closed circuit.

2.1.1. Phantom creation

The phantom creation was designed to replicate the flap pedicle within subcutaneous tissue, building on previous research conducted in our laboratory (Nomoni *et al* 2020, Karimpour *et al* 2024, Ferizoli *et al* 2024) The mechanical properties of the vessels were reproduced by mixing equal parts of Gel-00 (Polytek Development Corp., Easton, PA, USA) Part A and Part B with appropriate ratios of deadener (*D*) and hardener (*H*). The mixture was degassed in a vacuum chamber, and phantom vessels were fabricated by dipping a flexible shaft into the silicone blend and withdrawing it at a constant rate. The wall thickness (*d*) and outer diameter (OD) of the fabricated vessels were measured. Based on the degree of expansion in response to the appropriate internal pressure, ΔCSA and compliance were calculated to determine the optimal blend ratio for mimicking human vessels.

To simulate the surrounding tissue, a silicone matrix was prepared using PlatSil Gel-00 with a deadener ratio of 1, resulting in a Shore OO 25 hardness. This formulation was chosen to match the elastic properties of human thigh adipose tissue (Karimpour *et al* 2024), ensuring a physiologically relevant mechanical environment. Regarding optical properties, the silicone matrix was maintained in its transparent state without additional scattering agents. Four separate phantoms were cast with the artery and vein embedded at depths of 3, 9, 15, and 21 mm (figure 1(a)).

2.1.2. In vitro *cardiovascular system configuration*

The fabricated tissue phantom was incorporated into an *in vitro* vascular system, replicating the systemic circulation system of the human body. The phantom was positioned within a dedicated sensor casing to provide light shielding and to limit vibrations or movement caused by pulsation. A reflectance PPG sensor, featuring Red (660 nm) and Infrared (940 nm) LEDs, was placed on the underside of the phantom.

This sensor was connected to a custom dual-channel PPG acquisition system, developed by the Research Centre for Biomedical Engineering (RCBE) group at City St George's, University of London (Ferizoli *et al* 2023, Chan *et al* 2019) which operates at a sampling rate of 2000 Hz. The signals were displayed and recorded using LabVIEW (version 2023 Q1, National Instruments, Austin, Texas). The ambient light and temperature were intentionally maintained at a constant level to isolate pure pressure-induced morphological changes.

To simulate blood flow, a liquid composed of deionised water and methylene blue powder (Thermo Fisher Scientific, UK) (Cwalinski *et al* 2020, Ferizoli *et al* 2024) was circulated throughout the system using a pulsating pump (PD-1100, BDC Laboratories, Wheat Ridge, CO) operating at 60–65 bpm. The phantom vein was assumed to have minimal pulsation and was therefore connected to a closed circuit with adjustable internal pressure (figure 1(b)).

As there is a lack of published quantitative evidence on the specific internal pressure thresholds for the early stages of ischaemia and congestion in free flaps, these parameters were determined through direct consultation with (Saiga *et al* 2022). Based on his extensive clinical experience of conducting continuous internal pressure monitoring in more than 200 free flap feeding vessels, the appropriate internal pressure thresholds were established. Consequently, the arterial internal pressure was set to 40–80 mmHg for the normal and congested state and 25–50 mmHg for the ischaemic state, adjusted using a clamp within the circuit. The venous internal pressure was set to 10 mmHg for the normal and ischaemic states and 30 mmHg for the congested state, adjusted by injecting fluid through a valve using a syringe (figure 1(b)).

2.2. Signal processing and statistical analysis

For the acquired signals, the SNR was calculated from the raw data before preprocessing, and waveforms at depths and wavelengths where the SNR was at least 15 dB (Charlton *et al* 2025) in each state were selected (table 2). The signal quality was further evaluated using the Perfusion Index (AC/DC Ratio), using the AC component after preprocessing and the DC component before preprocessing.

PPG signal preprocessing was performed following a standard signal processing pipeline consisting of four sequential stages: (1) bandpass filtering, (2) artefact detection, (3) artefact removal, and (4) baseline correction.

To preserve the primary physiological components of PPG signals (cardiac-related frequency components) while removing high-frequency noise and low-frequency drift, a bandpass filter with cutoff frequencies of 0.5–10 Hz was applied (Goda *et al* 2024). A 4th-order Chebyshev Type II filter was employed for filter design (Liang *et al* 2018). The stopband attenuation was set to 40 dB, and zero-phase filtering (forward–backward filtering) was implemented to avoid phase distortion (Oppenheim and Schafer 2010).

Following filtering, artefacts were detected using the MAD (Median Absolute Deviation) method, a statistical outlier detection technique (Leys *et al* 2013). The modified Z-score was calculated as follows…

$$\text{Modified}\,Z-\text{score}=0.6745\times\frac{(\text{Xi}-\text{median})}{\text{MAD}}. \tag{1}$$

where MAD = median (|Xi—median|), and 0.6745 is the conversion factor from MAD to standard deviation under the assumption of normal distribution. Data points with an absolute modified Z-score exceeding 3.5 were identified as artefacts (Miller 1991).

Detected artefact points were replaced using linear interpolation (Ram *et al* 2012). Specifically, values at artefact positions were estimated by linear interpolation using valid signal points that were not identified as artefacts.

In this study, baseline estimation and correction were performed using the cubic spline interpolation method (Wang *et al* 2007, Jang *et al* 2014). First, the baseline component was estimated as the lower envelope of the signal using a moving minimum filter with a window size corresponding to approximately one cardiac cycle (0.8 s, 1600 sample points). Next, a cubic spline function was fitted to the estimated baseline points with a smoothing parameter of $s = 0.01 \times N$ (where N is the number of sample points) to obtain a smoothed baseline curve. Finally, the baseline-corrected PPG signal was obtained by subtracting this baseline curve from the original signal.

Through these preprocessing steps, high-quality signals with reduced noise and baseline variations were obtained for both Red and IR channel PPG signals.

PPG features were extracted from the pulse waves (figure 2, table 1) (Millasseau *et al* 2006).

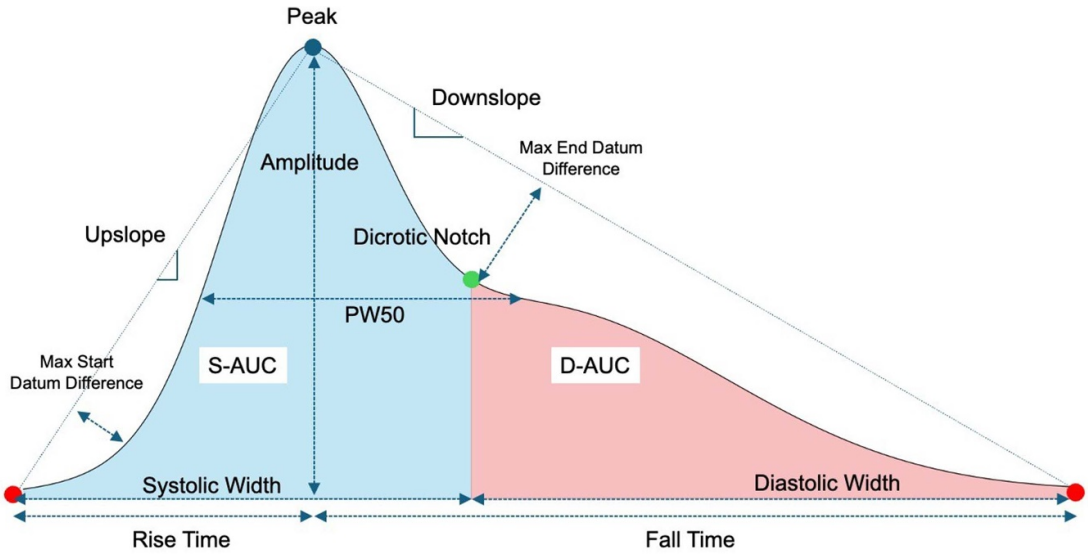

Figure 2. Example of PPG morphological features.

The diagnostic performance for differentiating the Normal, early Ischaemic, and early Congested states was evaluated using a comprehensive feature set. Receiver operating characteristic (ROC) analysis was performed for each pairwise comparison, wavelength, and depth to complement group-level p-values with a measure of diagnostic performance. Diagnostic accuracy was quantified by generating these ROC curves based on sensitivity and false-positive rates, with the area under the curve (AUC) serving as the final performance metric to quantify how well the normalised amplitude could distinguish between two states. To ensure the robustness of the AUC estimates, 95% confidence intervals (CIs) were derived using a bootstrap resampling method ($N = 1000$ resamplings). The distribution of AUC values across all depths and features was comprehensively evaluated to identify key parameters that exhibited characteristic responses to each haemodynamic state.

All statistical analyses and visualisations were performed in Python 3.13.0.

3. Results

3.1. Phantom fabrication and mechanical characterisation

The change in ΔCSA and compliance were calculated as shown in figure 3(a). The blend ratio for the arterial phantom was adjusted to approximate a ΔCSA range of 23.5%–25.9% and a compliance range of 1.3–3.52 $\times$ 10^{-4} cm^{-2} $mmHg^{-1}$ across pressure changes of 40–80 mmHg and 60–120 mmHg (Cappelletti *et al* 2022). The final ratio of the Hardener was determined to be 0.6, resulting in an initial internal diameter (ID_0) of 2.72 mm (figures 3(b) and (c)). Similarly, the blend ratio for the venous phantom was adjusted to approximate a ΔCSA range of 27.2%–41.8% and a compliance range of 5.6–17.4 $\times$ 10^{-4} cm^2 $mmHg^{-2}$ across pressure changes of 10–30 mmHg (Cappelletti *et al* 2022). The final ratio of the Deadener (D) was determined to be 0.4, resulting in an initial ID_0 of 3.19 mm (figures 3(d) and (e)). These artery and vein phantoms were then embedded 3, 9, 15, 21 mm deep within a subcutaneous tissue phantom (ratio of D was 1) created based on a previous report (Karimpour *et al* 2024, Falanga and Bucalo 1993 and Ferizoli *et al* 2024).

3.2. Signal acquisition

Across each wavelength, depth, and condition, the appropriate internal pressures were successfully replicated, and stable waveforms were acquired (figure 4). The waveforms were visualised with high quality.

3.3. Signal quality assessment

To assess signal quality, SNR was calculated for both raw and preprocessed data. Previous reports indicate that a high-quality signal typically has an SNR between 10 and 20 dB (Charlton *et al* 2025); the

Table 1. Table of 47 PPG features.

Category	Abbreviation	Definition
Combined (Red & IR))	PI_Ratio	Red PI divided by IR PI
	Amplitude_Ratio	Red amplitude divided by IR amplitude
	Delta_A_Ratio	Red absorbance change divided by IR absorbance change
Intensity	Amplitude	Peak-to-trough PPG amplitude
	PI	AC divided by DC, expressed as percentage
	Max_Start_Datum_Diff	Maximum vertical distance from onset to peak
	Max_End_Datum_Diff	Maximum vertical distance from end baseline to trough
	Median_Start_Datum_Diff	Median vertical distance from onset baseline to signal
	Median_End_Datum_Diff	Median vertical distance from end baseline to signal
Area	AUC	Total area under PPG curve per cycle
	S_AUC	Area from onset to dicrotic notch
	D_AUC	Area from dicrotic notch to next onset
	Start_Datum_Area	Area from onset baseline to systolic peak
	End_Datum_Area	Area from dicrotic notch baseline to pulse end
Time	Rise_Time	Duration from onset to systolic peak
	Decay_Time	Duration from systolic peak to next onset
	Pulse_Width	Total duration from onset to next onset
	PW50	Duration at 50% of peak amplitude
	Delta_T	Interval between vascular pulsatile noise (VPG) zero-crossings
	Systolic_Width	Duration from onset to dicrotic notch
	Diastolic_Width	Duration from dicrotic notch to next onset
	Rise_Decay_Time_Ratio	Rise time divided by decay time
Slope	Upslope	Maximum positive gradient during systolic rise
	Downslope	Maximum negative gradient during diastolic fall
	Onset_End_Slope	Average gradient from onset to next onset
	Upslope_Length	Arc length of systolic upstroke curve
	Downslope_Length	Arc length of diastolic downstroke curve
	Slope_Ratio	Upslope divided by downslope magnitude
	Length_Height_Ratio	Total arc length divided by pulse amplitude
	Slope_Length_Ratio	Upslope length divided by downslope length
	Upslope_Length_Ratio	Upslope arc length divided by total length
	Downslope_Length_Ratio	Downslope arc length divided by total length
SDPPG (Second Derivative PPG)	SDPPG_b_a	Early systolic negative peak divided by positive peak
	SDPPG_c_a	Late systolic re-increasing peak divided by early positive peak
	SDPPG_d_a	Late systolic re-decreasing peak divided by early positive peak
	SDPPG_e_a	Early diastolic positive peak divided by early systolic peak
	DNP	Dicrotic notch depth in second derivative
Shape & Stats	AUC_Ratio	Systolic area divided by diastolic area
	Datum_Area_Ratio	Start datum area divided by end datum area
	Width_Ratio	Systolic width divided by diastolic width
	Skewness	Third statistical moment quantifying asymmetry
	Kurtosis	Fourth statistical moment quantifying peakedness
	Variance	Second statistical moment quantifying variability
	Relative wave intensity (RWI)	Diastolic peak divided by systolic peak
	Inflection point area ratio (IPAR)	Area ratio at inflection point
	Zero crossing rate (ZCR)	Zero-crossing rate of first derivative
	Photoplethysmogram intensity ratio (PIR)	Pulse interval regularity measure

preprocessed signals in this study were consistent with this range. Because morphological analysis of the waveform requires higher signal integrity, only waveforms with a preprocessed SNR of 15 dB or higher across all states were selected for the analysis. These consisted of Red at 3 mm, and IR at 3 mm, 9 mm, and 15 mm. Furthermore, the calculated Perfusion Index (PI: AC/DC Ratio) was 0.13%–0.43% (table 2), which falls within the previously reported range of 0.12%–0.76% (Charlton *et al* 2025).

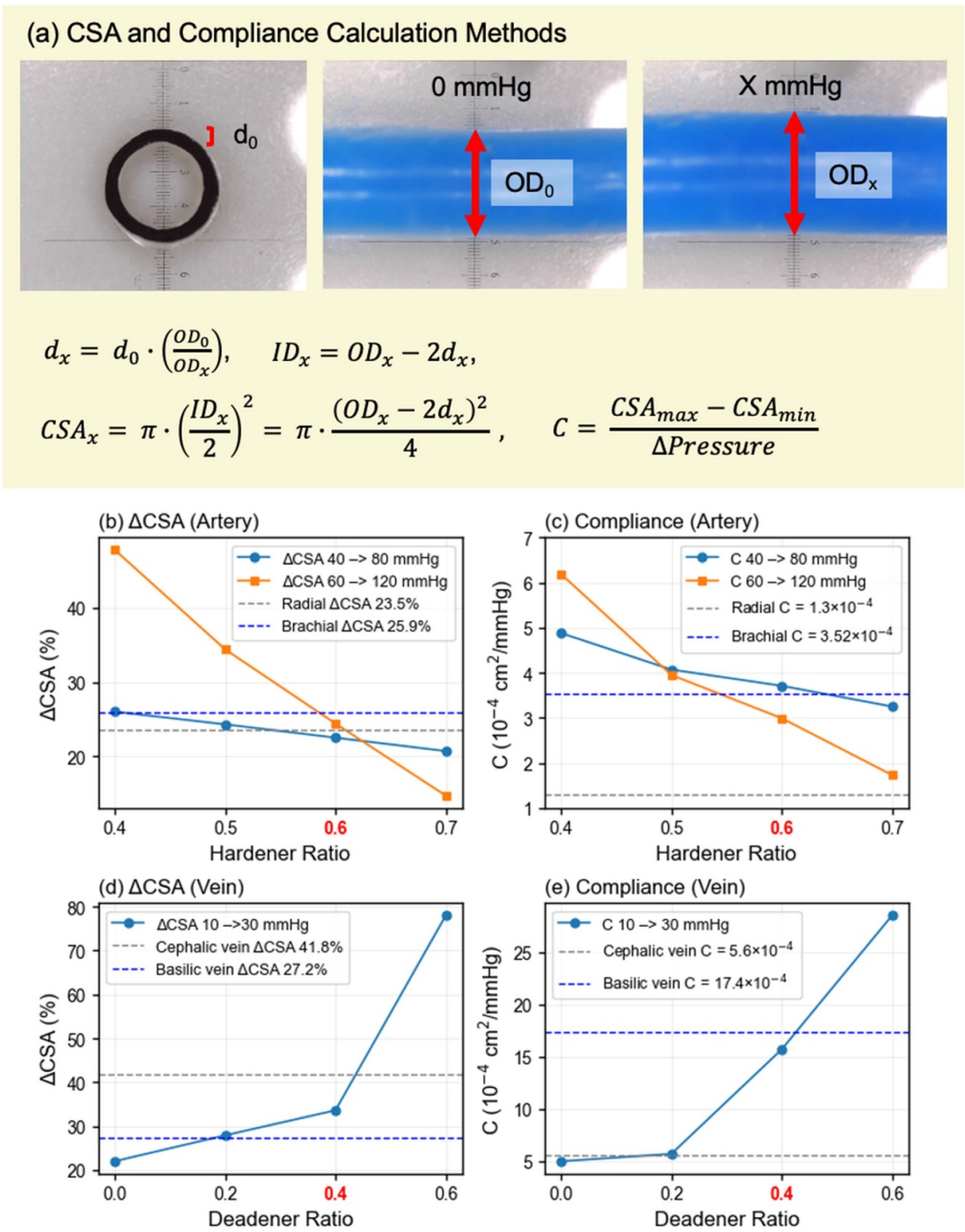

Figure 3. (a) Calculation of the mechanical properties of the created vascular phantom. (d): wall thickness, OD: outer diameter, ID: inner diameter, CSA: cross-sectional area, (c): compliance. (b) At hardener (H) = 0.6, the ΔCSA was 6.62–8.09 mm^{-2} (+22.5%) at 40–80 mmHg and 7.34–9.14 mm^2 (+24.4%) at 60–120 mmHg. (c) At $H = 0.6$, C was 3.71×10^{-4} cm^{-2} $mmHg^{-1}$ at 40–80 mmHg and 2.99×10^{-4} cm^{-2} $mmHg^{-1}$ at 60–120 mmHg. (d) At Deadener (d) = 0.4, ΔCSA was 9.36–12.5 mm^{-2} (+33.6%). (e) At $D = 0.4$, C was 15.7 × 10-4 cm^{-2} $mmHg^{-1}$ at 10–30 mmHg.

3.4. Diagnostic ability of each features

A total of 30 cardiac cycles were extracted and analysed per state (Normal, Ischaemia, and Congestion) at each depth and wavelength condition. The diagnostic performance of each feature was evaluated by calculating AUC for each depth and state, with the top 10 features presented in figure 5. Features exhibiting identical AUC values were grouped by category, with their specific components detailed in the legend below the plots. Red light was effective only for ischaemia at 3 mm, and the combination of Red and IR was useful for congestion at the same depth. In all other conditions, only IR was an effective wavelength. At 3 mm, a wide range of categories showed utility, with Intensity and Area being consistently useful. At 3 mm and 9 mm, Time-based features were also effective alongside Intensity and Area.

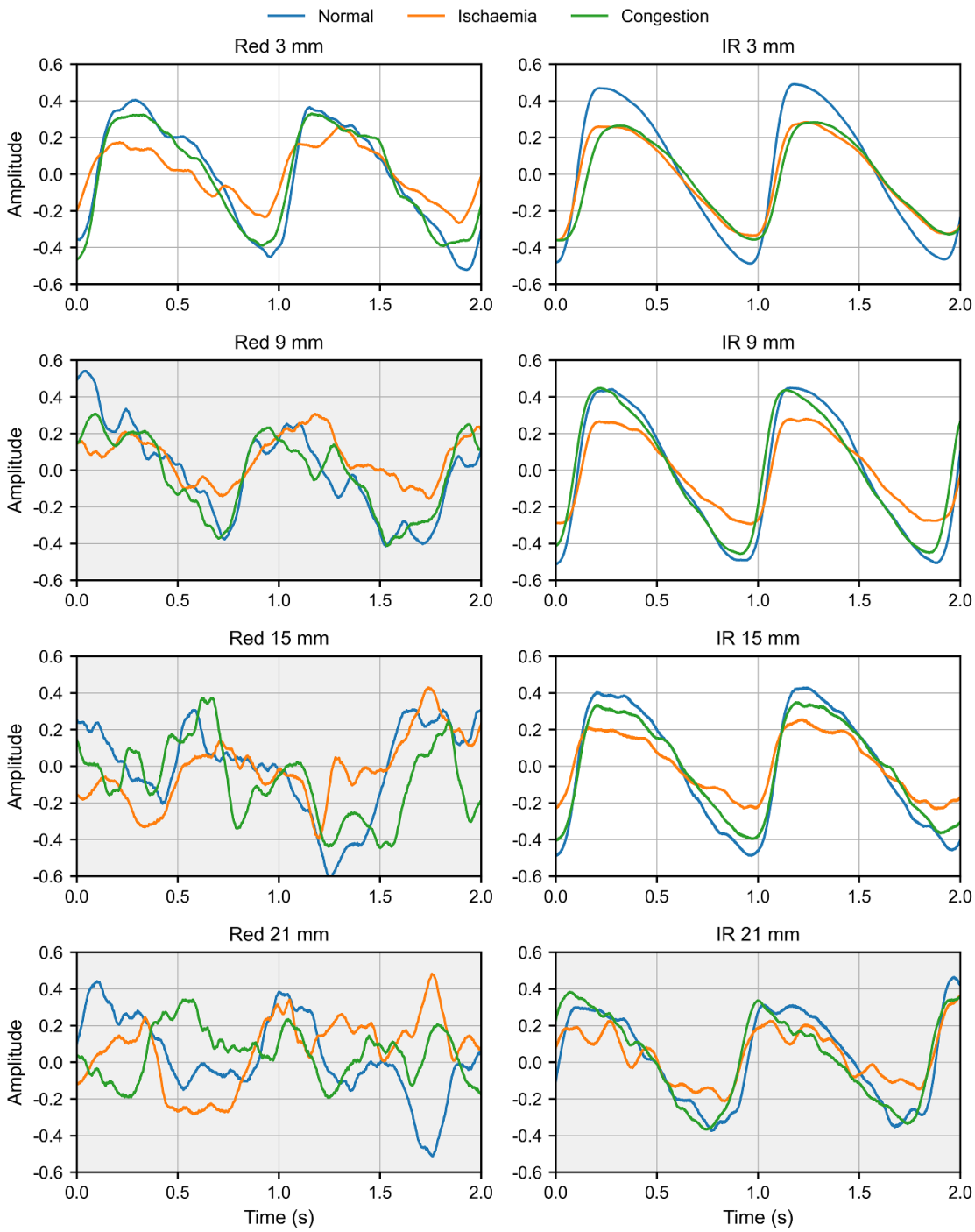

Figure 4. PPG waveforms for each wavelength and depth under normal, ischaemic, and congested conditions are presented. Among these, waveforms that maintained SNR exceeding 15 dB across all states (Red 3 mm, IR 3 mm, IR 9 mm, and IR 15 mm) were selected for the morphological analysis.

In contrast, at 15 mm, derivative features such as Slope and SDPPG showed the supplementary diagnostic value.

Furthermore, for the key features identified in figure 5, their relative changes across each depth and state were quantified. Figure 6 illustrates these variations as a ratio relative to the normal state (Normal = 1.0), providing a comparison of how each feature responds to different haemodynamic conditions. Values for features in the Intensity and Area categories were consistently ranked as Normal $\geqq$ Congestion $>$ Ischaemia. Indicators related to Time, Width, and Slope showed the most significant changes during ischaemia.

Table 2. Signal-to-noise ratio (SNR) and perfusion index (PI) at each depth.

Depth	State	Channel	SNR_Raw (dB)	SNR_Processed (dB)	PI (%)
3	Normal	Red	15.33	20.73	0.35
		IR	18.78	21.46	0.43
	Ischaemia	Red	11.26	17.3	0.22
		IR	17.36	20.62	0.39
	Congestion	Red	15.15	20.51	0.43
		IR	19.59	22.76	0.38
9	Normal	Red	6.7	15.04	0.17
		IR	17.93	21.43	0.21
	Ischaemia	Red	3.71	13.02	0.14
		IR	14.92	19.71	0.16
	Congestion	Red	7.91	15.93	0.18
		IR	17.96	21.56	0.22
15	Normal	Red	4.36	12.97	0.16
		IR	15.44	20.96	0.16
	Ischaemia	Red	1.33	10.71	0.15
		IR	11	18.74	0.13
	Congestion	Red	1.51	9.87	0.16
		IR	14.71	20.66	0.17
21	Normal	Red	3.42	12.78	0.18
		IR	11.17	19.99	0.16
	Ischaemia	Red	1.78	11.91	0.17
		IR	6.01	14.19	0.18
	Congestion	Red	3.2	11.97	0.19
		IR	12.75	20.9	0.14

4. Discussion

The required frequency for free flap assessment, with frequency as high as every hour to every 30 min (British Association of Plastic, Reconstructive and Aesthetic Surgeons *et al* 2012), has historically placed a substantial burden on healthcare systems, primarily relying on in-house resident physicians (Patel *et al* 2017). In the current environment, which prioritises strict limitations on working hours, this manual monitoring approach is reaching its practical limit (Patel *et al* 2017), creating a strong desire for reliable monitoring devices. Despite this, a culture of reliance on manual clinical checks persists.

Creech and Miller (Creech and Miller 1975) outlined the essential criteria for an effective flap perfusion monitoring system, requiring it to be accurate, reliable, applicable to all free flaps, easy for medical personnel to use, safe for both the patient and the flap, and capable of early detection. (Swartz *et al* 1988) further argued that an ideal monitoring method should provide continuous record patency and flow at the anastomosis, distinguish between arterial and venous compromise, and be applicable to both cutaneous and buried flaps.

A consistent feature across all free flap procedures, regardless of the presence of a skin paddle (the portion of skin included with the flap from the donor site), is the subcutaneous location of the pedicle (the nourishing vessels) and the relatively limited variation in its vessel calibre (Geoffrey Hallock 2009) (diameter of blood vessel). Our experimental design focused on developing a system that non-invasively accesses this pedicle, allowing for continuous measurement, discrimination between arterial and venous issues, and usability in buried flaps (transferred without a skin paddle, such as a muscle or bone flap, which is then covered by the native skin and is not visible on the surface).

The distinctive temporal window of blood flow compromise, with 80% of thrombosis occurring within two days post-surgery, 90% of arterial thrombosis within 24 h (Kroll *et al* 1996), and salvage rates dropping significantly after five hours (Bui *et al* 2007), is rarely seen in other disease groups. Developing a dedicated device focused solely on these tight parameters is commercially challenging due to the small

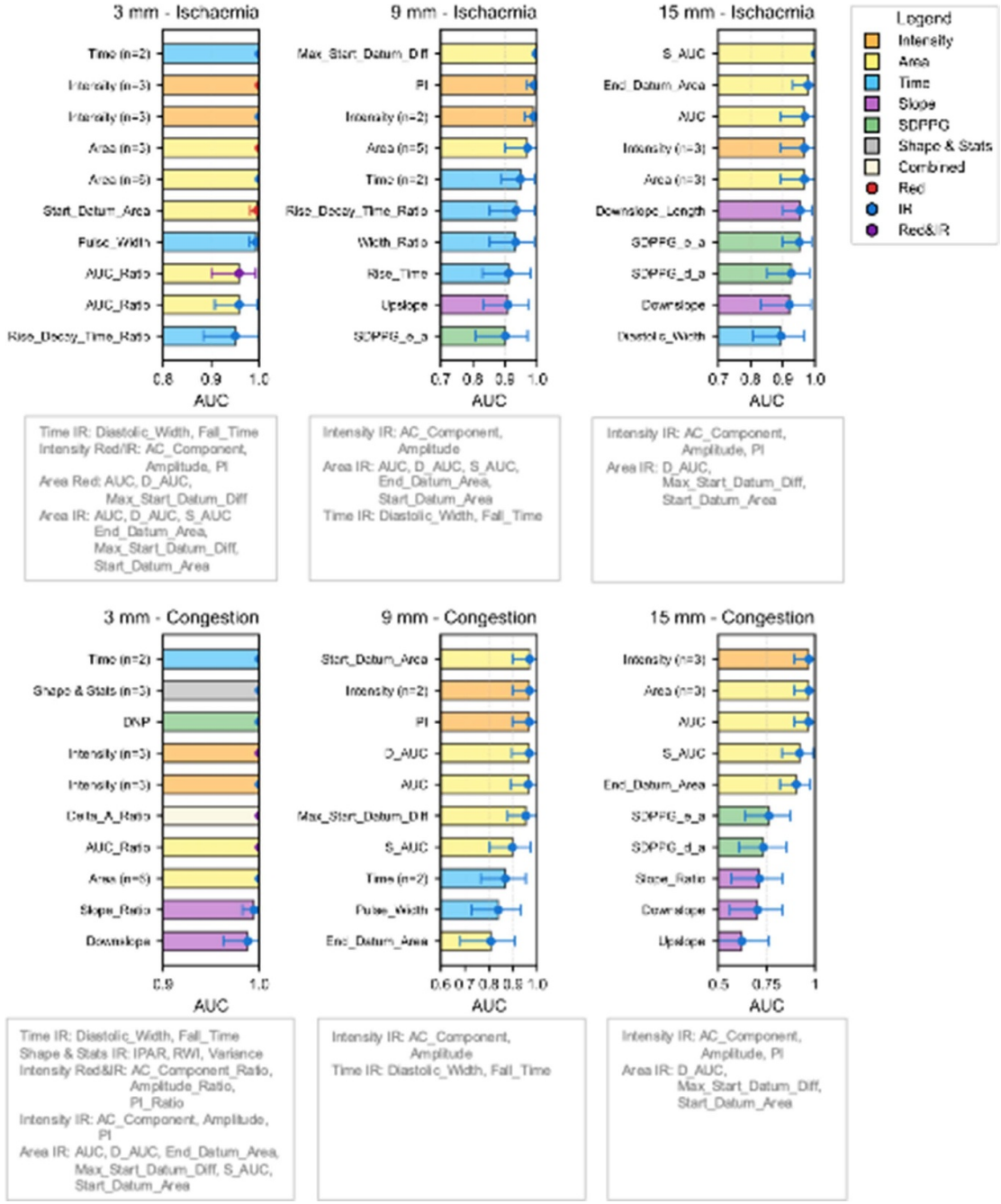

Figure 5. Diagnostic performance ranking based on AUC values across measurement depths and haemodynamic states. The top 10 features with the highest AUC values are presented for each depth (3, 9, and 15 mm) and condition (Ischaemia and Congestion). Features exhibiting identical AUC values are grouped into functional categories, with detailed breakdowns provided below each plot.

market size, thereby stifling innovation. Consequently, achieving 'commercially available' necessitates the application of established technological principles. In this context, PPG represents one of the most suitable technologies.

In this study, silicone vascular phantoms were first fabricated. To evaluate their mechanical properties, Young's modulus measurement and internal pressure testing were commonly considered. Internal pressure testing was chosen because it directly assessed compliance and the pressure–diameter relationship under conditions similar to physiological blood flow (Macrae *et al* 2016). In the internal pressure testing performed in this study, circumferential compliance was calculated, while longitudinal strain was not considered. This was because preliminary tests showed that when an internal pressure of 30 mmHg

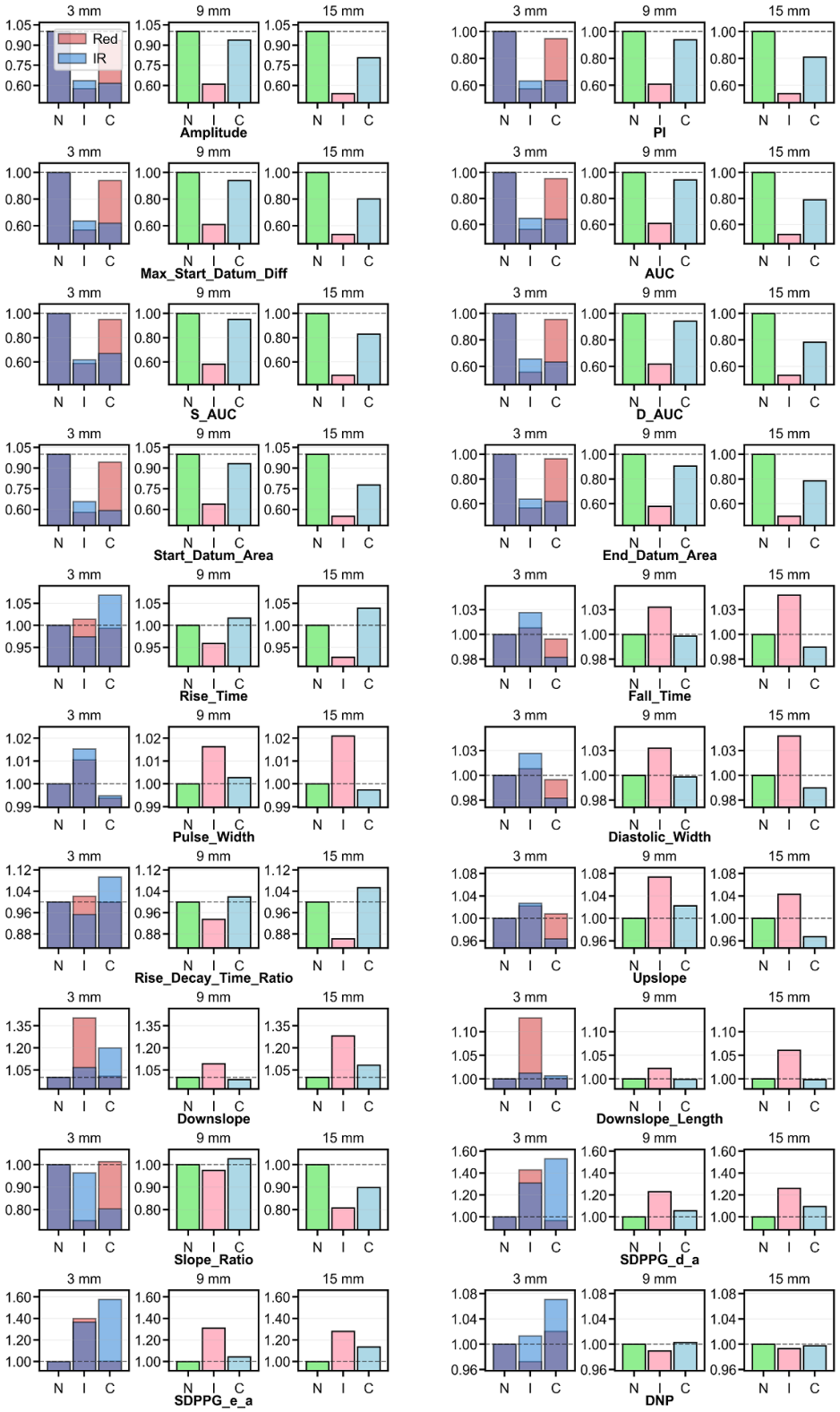

Figure 6. Relative changes in key diagnostic features compared to the normal state (*N*: Normal, *I*: Ischaemia, *C*: Congestion). The variations of the primary features identified in figure 5 are presented as ratios relative to the baseline (Normal = 1.0). Data are categorised by tissue depth (3, 9, and 15 mm) and haemodynamic state (Ischaemia and Congestion).

was applied to a soft silicone tube with a deadener ratio of 0.6, the axial elongation was only approximately 1%. The relationship between circumferential strain ($\varepsilon\theta$) and longitudinal strain (εz) can be expressed using Poisson's ratio (ν) as follows Pajic-lijakovic *et al* (2025):

$$\varepsilon\theta = \varepsilon z \cdot 2 \cdot \frac{1 - \nu/2}{1 - 2\nu}. \tag{2}$$

Since ν is approximately 0.49 for soft silicone, $\varepsilon\theta$ was calculated to be about 76 times greater than εz. Therefore, longitudinal strain was considered negligible.

The study also focused on whether the mechanical properties modulated by pneumatic pressure could be reliably reproduced within a tissue phantom with a softness equivalent to that of human adipose tissue. Assuming the Young's modulus (E) of the tissue phantom, adjusted to match human subcutaneous tissue, is equivalent to the reported value of 1.6 kPa (Alkhouli *et al* 2013), the resistive back-pressure against this internal pressure gradient is calculated using the following equation:

$$P_{\text{ext}} \approx \frac{E}{3}\left(1-\left(\frac{r_0}{r}\right)^2\right) \tag{3}$$

where r_0 and r are the initial and expanded radii, respectively, and $E/3$ represents the shear modulus, assuming ν of approximately 0.49. The resulting value of less than approximately 2–3 mmHg at this scale allows for the assumption that vessel expansion in the phantom is nearly identical to measurements in air.

The pressure range of 40–80 mmHg was set to simulate the internal thoracic artery, and 60–120 mmHg was used to simulate the radial artery. As expected, increasing the deadener ratio increased both ΔCSA and compliance, whereas increasing the hardener ratio had the opposite effect. The arterial model showed the best agreement with physiological artery behaviour at a hardener ratio of $H = 0.6$, where ΔCSA was 6.62–8.09 mm^{-2} (+22.5%) at 40–80 mmHg and 7.34–9.14 mm^{-2} (+24.4%) at 60–120 mmHg, which falls within reported values for the radial artery (3.4–4.2 mm^{-2}, + 23.5%) and brachial artery (8.1–10.2 mm^{-2}, + 25.9%) (Cappelletti *et al* 2022). The compliance of the arterial model (2.99×10^{-4} cm^{-2} mmHg^{-1}) was also comparable to reported physiological values for the radial (1.3×10^{-4} cm^{-2} mmHg^{-1}) and brachial arteries (3.52×10^{-4} cm^{-2} mmHg^{-1}) (Cappelletti *et al* 2022). In terms of scale, the cross-sectional area also matched the reported range for the deep inferior epigastric artery (3.14–9.62 mm^{-2}) (Ayhan *et al* 2009). Similarly, the venous model best reproduced physiological venous mechanics at a deadener ratio of $D = 0.4$, where ΔCSA was 9.36–12.5 mm^{-2} (+33.6%) at 10–30 mmHg, which lies between reported values for the cephalic vein (5.5–7.8 mm^{-2}, + 41.8%) and Basilic vein (16.9–21.5 mm^{-2}, + 27.2%) (Cappelletti *et al* 2022). The compliance of the venous model (15.7×10^{-4} cm^{-2} mmHg^{-1}) was also consistent with reported venous values for the cephalic (5.6×10^{-4} cm^{-2} mmHg^{-1}) and Basilic veins (17.4×10^{-4} cm^{-2} mmHg^{-1}) (Cappelletti *et al* 2022). In terms of scale, the cross-sectional area was consistent with the reported range for the deep inferior epigastric vein (0.20–14.50 mm^{-2}) (Ayhan *et al* 2009).

The calculated SNR values (10–20 dB) indicated consistent signal quality (Charlton *et al* 2025). While no formal minimum SNR exists for PPG morphology, pulsatile peaks remained distinct. Although dicrotic notches appeared less defined visually, computational analysis identified them at stable positions. This obscuration is typical in elderly patients and peripheral vasculature, representing common profiles in free flap monitoring where morphological analysis remains documented as acceptable (Elgendi 2016).

ROC confirmed that PPG features effectively distinguish vascular states, demonstrating their capacity to identify flap compromise through specific morphological characteristics.

Depth-specific performance revealed wavelength trends: Red light features were effective only in 3 mm ischaemia, consistent with its 3 mm penetration depth (Park *et al* 2021). For 3 mm congestion, while combined Red and IR indices also proved useful, IR features remained the primary markers for identifying haemodynamic changes across most other conditions. Nevertheless, these findings do not suggest that IR alone is sufficient for comprehensive monitoring. Since PPG signals are influenced by the subpapillary vascular plexus, superficial perfusion data obtained via Red remains essential, particularly when sensors are positioned on the skin paddle of a flap.

Intensity and area parameters performed well across all depths. At 3 mm, diverse categories showed potential. At 9 mm, time-based features were effective secondary markers. At 15 mm, amplitude attenuation favoured derivative parameters (slope, SDPPG), which offer higher sensitivity than time-based features.

The specific changes in feature values shown in figure 6 reveal a clear hierarchy of Normal $\geqslant$ Congestion $>$ Ischaemia for intensity and area-based parameters. This trend aligns with the expected physiological blood volume in each state. The variations in time-based features can be explained by changes in afterload. In ischaemia, reduced stroke volume leads to rapid completion of the systolic phase, followed by prolonged diastolic duration due to reduced tissue perfusion. In congestion, elevated venous pressure increases effective afterload, resulting in a prolonged anacrotic phase and shortened diastolic period. Furthermore, the significant changes observed in the SDPPG e/a and d/a ratios are consistent with their function as indices of peripheral vascular resistance (Park *et al* 2021).

Morphological PPG analysis provides an effective method for identifying early vascular complications in free flaps. This study characterises specific features and their variations that distinguish ischaemic and congested states, demonstrating PPG's capacity to differentiate arterial pump failure from venous outflow obstruction. Rather than clinical trials, phantom experiments were employed to validate PPG's diagnostic accuracy for early-stage changes. This approach is justified as human vascular compromise is rare and ethically difficult to induce, while animal models often present scale mismatches.

Several limitations remain in this study. First, the current phantom focuses on the main pedicle vessel, and the complexity of the subpapillary vascular plexus and capillary network was not replicated. *In vivo* PPG signals, including at red wavelengths (660 nm), arise from multiple vascular compartments. However, videocapillaroscopy studies suggest that individual capillaries exhibit limited cyclic diameter change in response to arterial pressure, and that the dominant contributors to the pulsatile (AC) component are pressure- and volume-induced changes in the deeper arteriolar and arterial vasculature (Volkov *et al* 2017). Nevertheless, the absence of a capillary network may influence specific waveform characteristics. For instance, the dicrotic notch, shaped by wave reflection and peripheral resistance throughout the distal arterial and arteriolar tree, may be attenuated or simplified in the phantom because terminal capillary bed resistance is not represented (Politi *et al* 2016). Furthermore, during venous congestion *in vivo*, progressive capillary engorgement produces a rising DC component and baseline drift that are unlikely to be fully reproduced by single-vessel occlusion alone. Future phantom designs incorporating a microvascular network analogue—such as arrays of micro-channels embedded in a scattering silicone matrix—would allow a more complete representation of *in vivo* PPG morphology across the vascular hierarchy.

Second, limitations exist regarding the fluid and optical properties of the in vitro model. The circulating fluid (deionised water mixed with methylene blue) is a Newtonian fluid, which does not replicate the complex non-Newtonian, shear-thinning behaviour of real blood resulting from erythrocyte aggregation and deformation. Although the lack of non-Newtonian properties may cause minor deviations in local haemodynamics, particularly in regions with low wall shear stress (Javid Mahmoudzadeh Akherat *et al* 2017), existing haemodynamic studies have demonstrated that the differences between Newtonian and non-Newtonian fluid models in macroscopic flow fields and overall pressure distributions are largely insignificant. Because the macroscopic pressure and volume fluctuations are the primary determinants of the overall PPG waveform features, the overall impact of using a Newtonian fluid is expected to be limited. However, potential deviations in specific waveform features due to the lack of non-Newtonian properties cannot be entirely ruled out (Liu *et al* 2021). Nonetheless, this gap from clinical reality should be acknowledged when directly extrapolating our in vitro haemodynamic responses to complex *in vivo* physiological conditions. Regarding optical properties, while the phantom mimics the softness of adipose tissue, the silicone remains transparent and does not account for the optical scattering of real skin or the light absorption of actual blood. Consequently, the light attenuation and effective sensing depth in this model may differ from those in vascularised human tissue. The 15 mm depth demonstrated here defines the potential theoretical limit of PPG rather than a direct clinical threshold. Incorporating scattering agents, such as titanium dioxide, or utilising artificial skin models is necessary for future validation to bridge this gap towards clinical applicability.

Third, structural and mechanical factors must be considered. The mechanical properties of the vessels were adjusted in air, which may differ from their behaviour when embedded in the silicone matrix, potentially suppressing vasodilation within the phantom. Longitudinal vessel strain was also treated as negligible. Crucially, the phantom is a complete composite block with no tissue interface space, failing to replicate postoperative complications such as haematoma accumulation that can compress the pedicle and compromise flap integrity. Additionally, in actual clinical scenarios, the acute postoperative inflammatory response causes fluid to shift into the third space, leading to local tissue oedema. Haematoma and oedema can compress the vascular pedicle (Ahmad *et al* 2015), potentially attenuating signal amplitude by restricting arterial expansion and decreasing the DC component baseline by impeding venous distension. Future research should evaluate models incorporating stepwise haematoma and oedema simulations.

Fourth, temperature variations in the clinical environment pose a significant challenge for PPG morphological analysis. In practice, patients are often cold initially and are subsequently warmed by external devices. Given that a temperature rise from 22 °C to 40 °C significantly elevates the AC component in 75% of subjects (Jeong *et al* 2014), this introduces the possibility that artificial heating could induce physiological vasodilation that elevates the AC component, potentially masking the early morphological changes or amplitude reductions typically associated with vascular compromise. To minimise the risk of overlooking delayed vascular thrombosis, future monitoring systems should consider integrating local temperature sensors and temperature-compensation algorithms to account for these variations.

Finally, the pressure thresholds for early haemodynamic compromise were established based on clinical experience due to a lack of published quantitative standards. The clinical influence of external factors, such as different skin colours, sensor contact pressure, and ambient light, also needs further study. Despite these limitations, this study holds considerable value as a foundational prototype and one of the few investigations specifically addressing a free flap phantom. By isolating the pure morphological changes caused by internal pressure-driven vasodilation and identifying the limits of measurable PPG depth under controlled conditions, these findings serve as a crucial reference point. Understanding how each isolated factor directly affects the PPG signal provides a vital framework for decoding more complex physiological signals, guiding the future development of highly reproducible models for clinical translation.

5. Conclusion

In light of recent advancements in PPG technology, an *in vitro* setting capable of simulating normal, ischaemic, and congested states serves as a valuable tool for research in free flap monitoring. The objectives of this study were twofold: (1) to develop a custom-made silicone phantom that simulates a free flap with reproducible ischaemic and congested states, and (2) to verify the diagnostic capability of PPG through morphological analysis at each depth.

PPG signals obtained from this model were recorded and analysed to identify specific morphological features and their characteristic value variations associated with early flap disorder. These findings suggest that incorporating morphological analysis can improve the accuracy of conventional optical sensor-based flap monitoring, providing a more reliable approach to detecting blood flow impairment.

Acknowledgment

This research was supported by the Pump Priming Funds for consumables awarded by the British Association of Plastic, Reconstructive and Aesthetic Surgeons (BAPRAS). The authors would like to express their sincere gratitude to BAPRAS for the financial support that made this work possible.

I sincerely thank Dr Saiga for his profound knowledge and expert guidance on setting the precise internal arterial and venous pressure parameters for the in vitro experiments, drawing from his extensive experience with over 200 cases of continuous catheter-based pressure monitoring in free flaps. I also wish to thank my laboratory colleagues for laying the foundational work of this research and my colleagues who assisted with the waveform quality assessment.

This research was supported by the Pump Priming Funds for consumables awarded by the British Association of Plastic, Reconstructive and Aesthetic Surgeons (BAPRAS).

Data availability statement

The datasets generated during and/or analysed during the current study are available from the corresponding author on reasonable request.

The data that support the findings of this study are openly available at the following URL/DOI: https://github.com/Hiroki-Kodama-PRS/Phantom-analysis/tree/main/Physiological%20Measurement.

Author contributions

Hiroki Kodama 0009-0005-3970-0770

Conceptualization (equal), Data curation (equal), Formal analysis (equal), Investigation (equal), Methodology (equal), Project administration (equal), Resources (equal), Software (equal), Validation (equal), Visualization (equal), Writing – original draft (equal), Writing – review & editing (equal)

James M May 0000-0002-8659-756X
Supervision (equal)

Dariush Nikkhah
Funding acquisition (equal), Supervision (equal), Writing – review & editing (equal)

Panicos A Kyriacou
Supervision (equal)

References

Ahmad F I, Gerecci D, Gonzalez J D, Peck J J and Wax M K 2015 The role of postoperative hematoma on free flap compromise *Laryngoscope* **125** 1811–5
Al-dam A, Zrnc T A, Hanken H, Riecke B, Eichhorn W, Nourwali I, Smeets R, Blessmann M, Heiland M and Gröbe A 2014 Outcome of microvascular free flaps in a high-volume training centre *J. Craniomaxillofac. Surg.* **42** 1178–83
Alkhouli N *et al* 2013 The mechanical properties of human adipose tissues and their relationships to the structure and composition of the extracellular matrix *Am. J. Physiol. Endocrinol. Metab.* **305** E1427–E1435
American Society of Plastic Surgeons 2020 (available at: www.plasticsurgery.org/documents/news/statistics/2020/plastic-surgery-statistics-full-report-2020.pdf) (Accessed 13 October 2025)
Ayhan S, Oktar S O, Tuncer S, Yucel C, Kandal S and Demirtas Y 2009 Correlation between vessel diameters of superficial and deep inferior epigastric systems: Doppler ultrasound assessment *J. Plast. Reconstr. Aesthet. Surg.* **62** 1140–7
Budidha K, Rybynok V and Kyriacou P A 2018 Design and development of a modular, multichannel photoplethysmography system *IEEE Trans. Instrum. Meas.* **67** 1954–65
Bui D T, Cordeiro P G, Hu Q Y, Disa J J, Pusic A and Mehrara B J 2007 Free flap reexploration: indications, treatment, and outcomes in 1193 free flaps *Plast. Reconstr. Surg.* **119** 2092–100
Burnier P, Niddam J, Bosc R, Hersant B and Meningaud J P 2017 Indocyanine green applications in plastic surgery: a review of the literature *J. Plast. Reconstr. Aesthet. Surg.* **70** 814–27
British Association of Plastic, Reconstructive and Aesthetic Surgeons 2012 Oncoplastic breast reconstruction guidelines for best practice (available at: www.bapras.org.uk/docs/default-source/commissioning-and-policy/final-oncoplastic-guidelines---healthcare-professionals.pdf?sfvrsn=0)
Caine P, Jeevaratnam J A, Misky A and Nikkhah D 2023 Post-operative monitoring *Core Techniques in Flap Reconstructive Microsurgery—A Stepwise Guide* (Springer) pp 39–46
Cappelletti S, Caimi A, Caldiroli A, Baroni I, Votta E, Riboldi S A, Marrocco-trischitta M M, Redaelli A and Sturla F 2022 Non-invasive estimation of vascular compliance and distensibility in the arm vessels: a novel ultrasound-based protocol *Quant. Imaging Med. Surg.* **12** 3515–27
Chan G *et al* 2019 Multi-site photoplethysmography technology for blood pressure assessment: challenges and recommendations *J. Clin. Med.* **8** 1827
Charlton P H *et al* 2023 The 2023 wearable photoplethysmography roadmap *Physiol. Meas.* **44** 111001
Charlton P H, Marozas V, Mejía-mejía E, Kyriacou P A, Mant J and Karlen W 2025 Determinants of photoplethysmography signal quality at the wrist *PLOS Digit. Health.* **4** e0000585
Chen K-T, Mardini S, Chuang D C-C, Lin C-H, Cheng M-H, Lin Y-T, Huang W-C, Tsao C-K and Wei F-C 2007 Timing of presentation of the first signs of vascular compromise dictates the salvage outcome of free flap transfers *Plast. Reconstr. Surg.* **120** 187–95
Colakoglu S, Johnson A, Anderson J, Mathes D W and Chong T W 2020 Changes to venous flow coupler signal during Diep flap inset can be predictive of poor clinical outcomes in autologous breast reconstruction *J. Reconstr. Microsurg.* **36** 466–70
Creech B and Miller S 1975 Evaluation of circulation in skin flaps *Skin Flaps* (Little, Brown and Company) pp 21
Cwalinski T, Polom W, Marano L, Roviello G, D'angelo A, Cwalina N, Matuszewski M, Roviello F, Jaskiewicz J and Polom K 2020 Methylene blue-current knowledge, fluorescent properties, and its future use *J. Clin. Med.* **9** 3538
Disa J J, Cordeiro P G and Hidalgo D A 1999 Efficacy of conventional monitoring techniques in free tissue transfer: an 11-year experience in 750 consecutive cases *Plast. Reconstr. Surg.* **104** 97–101
Elgendi M 2016 Optimal signal quality index for photoplethysmogram signals *Bioengineering* **3** 21
Falanga V and Bucalo B 1993 Use of a durometer to assess skin hardness *J. Am. Acad. Dermatol.* **29** 47–51
Ferizoli R, Karimpour P, May J M and Kyriacou P A 2023 A bilateral in vitro model for cardiovascular disease investigations using photoplethysmography sensors*2023 IEEE BioSensors Conf. (Biosensors)* (IEEE) pp 1–4
Ferizoli R, Karimpour P, May J M and Kyriacou P A 2024 Arterial stiffness assessment using PPG feature extraction and significance testing in an in vitro cardiovascular system *Sci. Rep.* **14** 2024
Geoffrey Hallock G 2009 Chapter 3: flap selection *Flaps and Reconstructive Surgery* (Elsevier) pp 17
Goda M Á, Charlton P H and Behar J A 2024 pyPPG: a Python toolbox for comprehensive photoplethysmography signal analysis *Physiol. Meas.* **45** 045001
Harashina T, Imai T, Nakajima H and Fujino T 1980 Breast reconstruction with microsurgical free composite tissue transplantation *Br. J. Plast. Surg.* **33** 30–37
Hudson T, Hogue E, Mullner D, Herrera F and Scomacao I 2023 The utility of smartphone-based thermal imaging in the management and monitoring of microvascular flap procedures: a systematic review and meta-analysis *Ann. Plast. Surg.* **90** S420–S425
Hwang S J 2023 Diagnostic accuracy of microdialysis in postoperative flap monitoring *J. Craniofac. Surg.* **34** 288–90
Jang D G, Park S, Hahn M and Park S H 2014 A real-time pulse peak detection algorithm for the photoplethysmogram *Int. J. Electron. Electr. Eng.* **2** 45–49
Javid Mahmoudzadeh Akherat S M, Cassel K, Boghosian M, Dhar P and Hammes M 2017 Are non-Newtonian effects important in hemodynamic simulations of patients with autogenous fistula? *J. Biomech. Eng.* **139** 044504
Jeong I C, Yoon H, Kang H and Yeom H 2014 Effects of skin surface temperature on photoplethysmograph *J. Healthc. Eng.* **5** 429–38
Kagaya Y and Miyamoto S 2018 A systematic review of near-infrared spectroscopy in flap monitoring: current basic and clinical evidence and prospects *J. Plast. Reconstr. Aesthet. Surg.* **71** 246–57

Karimpour P, Ferizoli R, May J M and Kyriacou P A 2024 Customisable silicone vessels and tissue phantoms for in vitro photoplethysmography investigations into cardiovascular disease *Sensors* **24** 1681
Kodama Hiroki 2026 Phantom-analysis (available at: https://github.com/Hiroki-Kodama-PRS/Phantom-analysis/tree/main/Physiological%20Measurement)
Kodama H, Ishida K, Hirayama H, Orgun D, Kawashima K, Nikkhah D, May J, Kyriacou P A and Miyawaki T 2025 The future of free flap monitoring by laser continuous Doppler flowmetry: a prospective assessment in consecutive 71 patients *JPRAS Open.* **43** 140–52
Kroll S S, Schusterman M A, Reece G P, Miller M J, Evans G R D, Robb G L and Baldwin B J 1996 Timing of pedicle thrombosis and flap loss after free-tissue transfer *Plast. Reconstr. Surg.* **98** 1230–3
Kwasnicki R M, Noakes A J, Banhidy N and Hettiaratchy S 2021 Quantifying the limitations of clinical and technology-based flap monitoring strategies using a systematic thematic analysis *Plast. Reconstr. Surg. Glob. Open.* **9** e3663
Kyriacou P A 2022 *Photoplethysmography: Technology, Signal Analysis and Applications* (Elsevier)
Kyriacou P A, Zaman T and Pal S K 2020 Photoplethysmography in postoperative monitoring of deep inferior epigastric perforator (DIEP) free flaps *Physiol. Meas.* **41** 124001
Leys C, Ley C, Klein O, Bernard P and Licata L 2013 Detecting outliers: do not use standard deviation around the mean, use absolute deviation around the median *J. Exp. Soc. Psychol.* **49** 764–6
Liang Y, Chen Z, Ward R and Elgendi M 2018 Photoplethysmography and deep learning: enhancing hypertension risk stratification *Biosensors* **8** 101
Liu H *et al* 2021 Comparison of Newtonian and non-Newtonian fluid models in blood flow simulation in patients with intracranial arterial stenosis *Front. Physiol.* **12** 718540
Macrae R A, Miller K and Doyle B J 2016 Methods in mechanical testing of arterial tissue: a review *Strain* **52** 380–99
Mericli A F, Wren J, Garvey P B, Liu J, Butler C E and Selber J C 2017 A prospective clinical trial comparing visible light spectroscopy to handheld Doppler for postoperative free tissue transfer monitoring *Plast. Reconstr. Surg.* **140** 604–13
Millasseau S C, Ritter J M, Takazawa K and Chowienczyk P J 2006 Contour analysis of the photoplethysmographic pulse measured at the finger *J. Hypertens.* **24** 1449–56
Miller J 1991 Short report: reaction time analysis with outlier exclusion: bias varies with sample size *Q. J. Exp. Psychol. A.* **43** 907–12
Nakatsuka T, Harii K, Asato H, Takushima A, Ebihara S, Kimata Y, Yamada A, Ueda K and Ichioka S 2003 Analytic review of 2372 free flap transfers for head and neck reconstruction following cancer resection *J. Reconstr. Microsurg.* **19** 363–8
Nomoni M, May J M and Kyriacou P A 2020 Novel polydimethylsiloxane (PDMS) pulsatile vascular tissue phantoms for the *in-vitro* investigation of light tissue interaction in photoplethysmography *Sensors* **20** 4246
Oppenheim A V and Schafer R W 2010 *Discrete-Time Signal Processing* (Pearson) (available at: https://books.google.co.uk/books?id=mYsoAQAAMAAJ)
Pajic-lijakovic I, Milivojevic M and McClintock P V E 2025 Compressibility of biological systems: the viscoelastic Poisson's ratio *Adv. Phys.* **10** 2440023
Park J, Seok H S, Kim S S and Shin H 2021 Photoplethysmogram analysis and applications: an integrative review *Front. Physiol.* **12** 808451
Patel U A *et al* 2017 Free flap reconstruction monitoring techniques and frequency in the era of restricted resident work hours *JAMA Otolaryngol. Head Neck Surg.* **143** 803
Politi M T, Ghigo A, Fernández J M, Khelifa I, Gaudric J, Fullana J M and Lagrée P-Y 2016 The dicrotic notch analyzed by a numerical model *Comput. Biol. Med.* **72** 54–64
Ram M R, Madhav K V, Krishna E H, Komalla N R and Reddy K A 2012 A novel approach for motion artifact reduction in PPG signals based on AS-LMS adaptive filter *IEEE Trans. Instrum. Meas.* **61** 1445–57
Saiga A, Kubota Y, Yamaji Y and Mitsukawa N 2022 Intraflap vascular catheterization method for monitoring, prevention, and intervention of thrombogenesis in free-flap surgery *Ann. Plast. Surg.* **88** 68–73
Swartz W M, Jones N F, Cherup L and Klein A 1988 Pittsburgh direct monitoring of microvascular anastomoses with the 20-MHz ultrasonic Doppler probe: an experimental and clinical study *Plast. Reconstr. Surg.* **81** 149–58
Taylor G I, Miller G D H and Ham F J 1975 The free vascularized bone graft: a clinical extension of microvascular techniques *Plast. Reconstr. Surg.* **55** 533–44
Tran N V, Buchel E W and Convery P A 2007 Microvascular complications of DIEP flaps *Plast. Reconstr. Surg.* **119** 1397–405
Volkov M V, Margaryants N B, Potemkin A V, Volynsky M A, Gurov I P, Mamontov O V and Kamshilin A A 2017 Video capillaroscopy clarifies mechanism of the photoplethysmographic waveform appearance *Sci. Rep.* **7** 13298
Wang L, Lo B P and Yang G Z 2007 Multichannel reflective PPG earpiece sensor with passive motion cancellation *IEEE Trans. Biomed. Circuits Syst.* **1** 235–41
Wu K G, Chong C T, Hanlon H, Langenfeld T L, Johnson R M, Crawford T N, Wax M K and Kadakia S P 2023 Implantable arterial Doppler efficacy in free flap reconstruction: a systematic review and meta-analysis *Head Neck* **45** 2710–7
Zaman T, Kyriacou P A and Pal S K 2011 Development of a reflectance photoplethysmographic sensor used for the assessment of free flap perfusion *2011 Annual Int. Conf. of the IEEE Engineering in Medicine and Biology Society* (IEEE) 2011 4006–9